

ROTATIONAL KINEMATICS IN THE GLOBULAR CLUSTER SYSTEM OF M31:
INSIGHTS FROM BAYESIAN INFERENCEYUAN (CHER) LI¹, BRENDON J. BREWER¹, GERAINT F. LEWIS², DOUGAL MACKEY³¹Department of Statistics, The University of Auckland, Private Bag 92019, Auckland 1142, New Zealand²Sydney Institute for Astronomy, School of Physics, A28, The University of Sydney, NSW 2006, Australia and³Independent researcher, Charnwood, Canberra, ACT 2615, Australia*Version January 14, 2026*

ABSTRACT

As ancient stellar systems, globular clusters (GCs) offer valuable insights into the dynamical histories of large galaxies. Previous studies of GC populations in the inner and outer regions of the Andromeda Galaxy (M31) have revealed intriguing subpopulations with distinct kinematic properties. Here, we build upon earlier studies by employing Bayesian modelling to investigate the kinematics of the combined inner and outer GC populations of M31. Given the heterogeneous nature of the data, we examine subpopulations defined by GCs' metallicity and by associations with substructure, in order to characterise possible relationships between the inner and outer GC populations. We find that lower-metallicity GCs and those linked to substructures exhibit a common, more rapid rotation, whose alignment is distinct from that of higher-metallicity and non-substructure GCs. Furthermore, the higher-metallicity GCs rotate in alignment with Andromeda's stellar disk. These pronounced kinematic differences reinforce the idea that different subgroups of GCs were accreted to M31 at distinct epochs, shedding light on the complex assembly history of the galaxy.

1. INTRODUCTION

Formed in the early epochs of the universe, globular clusters (GCs) offer valuable insights into the properties and formation of galaxies (Forbes et al. 2018; Beasley 2020). Given its proximity, the GCs population of the Andromeda Galaxy (M31) has the promise of revealing the accretion history of a large galaxy, shedding light on galactic growth in the local environment, including the life of our own Milky Way.

Separate studies of the kinematics and spatial distribution of GCs in the outer and inner regions of Andromeda have revealed a complex picture of distinct accretion events, some relatively recent and others more ancient (e.g. Mackey et al. 2019b; Lewis et al. 2023). Intriguingly, these suggest a possible causal relationship between the structures found in the outer and inner halo. We therefore aim to investigate the kinematic characteristics of M31's combined GC population (inner and outer GCs) to assess whether this combined approach supports a coherent picture of Andromeda's accretion history.

At ~ 765 kpc, M31 is the closest large neighbour to the Milky Way (Riess et al. 2012), and with a mass of $1.5 \times 10^{12} M_{\odot}$ (Peñarrubia et al. 2014), M31 is $\sim 30\%$ more massive. Almost 500 GCs associated with M31 have been identified out to ~ 150 kpc (e.g. Barmby & Huchra 2001; Mackey et al. 2010). This substantial GC system likely reflects not only M31's higher mass but also its more complex assembly and accretion history, which distinguishes it from the Milky Way. This is significantly larger than the Milky Way's GC population, consistent with the larger mass of M31 and the substantial intrinsic scatter in the relation between GC population size and host galaxy mass (Harris et al. 2013). This rich population of GCs has long attracted considerable interest (Crampton et al. 1985; Elson & Walterbos 1988), with Mackey et al. (2007) comparing the features of M31's

and the Milky Way's outer halo (15 kpc $\lesssim R_p$ (projected radii) $\lesssim 100$ kpc) GCs. Their findings imply that the outer halo of M31 has a greater number of metal-poor, more centrally concentrated, and highly luminous GCs than the Milky Way. Many other studies have compared the properties between the Milky Way and M31 (e.g. Kavelaars & Hanes 1997; Ibata et al. 2007; Beasley et al. 2004; Burstein et al. 2004; Schiavon et al. 2012). These point to M31's accretion history differing from the Milky Way's, potentially involving complex merger histories (Akib et al. 2025b,a).

Mackey et al. (2010) modelled the spatial distribution of GCs in the halo of M31 using a sample of 61 observed GCs from PAndAS (the Pan-Andromeda Archaeological Survey; McConnachie et al. 2009). Focusing primarily on GCs beyond $R_p = 30$ kpc (M31's outer halo), they found that these clusters are associated with underlying tidal debris features and exhibit a roughly isotropic spatial distribution. This finding was later confirmed by Mackey et al. (2012), who demonstrated that the correlation between outer halo GCs and tidal debris persists when considering the full PAndAS sample. Furthermore, Mackey et al. (2012) asserted that over 80% of M31's outer halo GCs were acquired through the accretion of satellite host galaxies. However, the findings of Mackey et al. (2019a) suggest that, at $R_p > 25$ kpc, approximately 35% to 62% of GCs show signs of having been accreted onto M31's halo. This discrepancy may arise from Mackey et al. (2012) analysing only 79 GCs of M31's outer halo compared to the 92 outer halo GCs studied by Mackey et al. (2019a).

Veljanoski et al. (2014) demonstrated that the outer halo GC population (those at $R_p > 30$ kpc) rotates along the same axis as the stellar disk of M31, albeit with a lower amplitude of 86 ± 17 km s $^{-1}$. For comparison, the disk rotation velocity is ~ 226 km s $^{-1}$ between 20 and 35 kpc (Carignan et al. 2006), indicating that the outer halo

TABLE 1
PRIOR PROBABILITY DISTRIBUTIONS FOR THE UNKNOWN PARAMETERS FOR MODEL 1.

Parameter	Description	Prior
σ (km s $^{-1}$)	Velocity dispersion	Uniform(0, 1000)
A (km s $^{-1}$)	Rotational Amplitude	Uniform(0, 1000)
ϕ (degrees)	Orientation of rotation axis	Uniform(-180, 180)

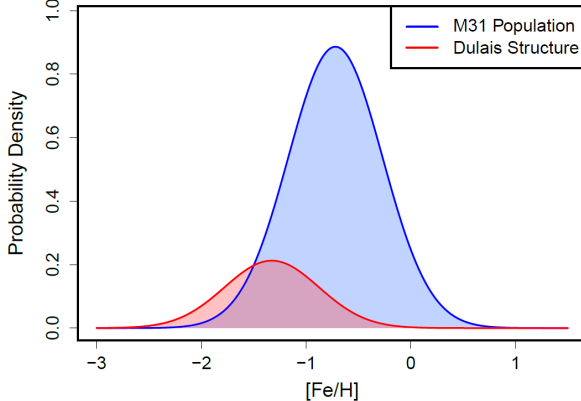


FIG. 1.— Schematic representation of the metallicity distribution of M31’s inner globular cluster population ($R_p < 25$ kpc, shown in blue) and of the Dulais Structure subset (shown in red), identified by Lewis et al. (2023) using the lowest metallicity inner GCs. While the populations would actually overlap as illustrated here, our modelling uses the simplifying assumption that the overall GC population is neatly split into two at a critical value of metallicity.

GCs rotate at roughly 38% of the disk’s rotational speed. Additionally, they identified a decline in velocity dispersion as a function of projected distance from M31’s centre, providing further evidence of the complex kinematic structure of the galaxy’s halo. Mackey et al. (2019b) investigated how the rotational properties of outer halo (GCs) in M31 vary depending on their association with substructures. Their findings revealed that GCs linked to substructures and those unassociated with them rotate in perpendicular orientations. There is compelling evidence (Mackey et al. 2019a,b) suggesting that GCs not located on substructures share similarities with ancient dwarf galaxies that accreted into M31’s halo approximately 12 Gyr ago (Johnston et al. 2008). In contrast, GCs associated with substructures are likely to have been accreted more recently (McConnachie et al. 2018), Gyr after the initial accretion events of the non-substructure GCs (Mackey et al. 2019b).

Beyond studies of the outer halo GCs, investigations of inner halo GCs have also provided critical insights into M31’s structure. Caldwell & Romanowsky (2016) conducted a comprehensive spatial-kinematic-metallicity analysis of GCs within a restricted radius of $R_p = 21$ kpc. By classifying GCs into three groups based on metallicity, they concluded that the system of higher metallicity GCs ($[\text{Fe}/\text{H}] > -0.4$) exhibit rotational velocity, velocity dispersion, and spatial properties akin to M31’s stellar disk. Conversely, the system of lower metallicity GCs ($[\text{Fe}/\text{H}] < -1.5$) were the least correlated with the disk, displaying moderately prograde rotation and a higher velocity dispersion. Furthermore, Lewis et al. (2023) found that certain rotational patterns of inner halo GCs (those with a lower metallicity — part of what they called the ‘Dulais structure’ after a Welsh river) align closely with those of outer halo GCs, suggesting a common progenitor or origin. The metallicity distribution of the inner GCs

TABLE 2
SUMMARY TABLE OF PARAMETER ESTIMATES FOR MODEL 1.

Parameter	Estimate
σ (km s $^{-1}$)	$137.66^{+5.54}_{-5.11}$
A (km s $^{-1}$)	$68.74^{+9.95}_{-10.31}$
ϕ (degrees)	$37.45^{+9.73}_{-9.58}$
PA (degrees)	$307.45^{+9.73}_{-9.58}$
A/σ ratio	$0.50^{+0.07}_{-0.08}$

and those associated with the Dulais Structure is illustrated schematically in Figure 1, showing that the latter dominates at low metallicity. While the two populations would overlap in reality, our modelling assumptions simplify matters by assuming that a critical metallicity value neatly divides the GC population into two parts, following Lewis et al. (2023).

The structure of the paper is as follows: Section 2 describes the data used in this current study. Section 3 discusses the kinematic models applied to examine the GC population of the M31 galaxy, with Bayesian inference used to determine the posterior probability distributions for the model parameters and the models’ marginal likelihoods (evidence). Finally, the discussion and conclusions are presented in Section 5.

2. DATA

The dataset used in this paper, which initially contained 422 GCs, is from a publicly available catalogue (Caldwell & Romanowsky 2016). Of the 422 clusters, 345 are from M31’s inner region ($R_p < 25$ kpc), whereas 77 are from the outer region. The data encompassing a majority of the known inner GCs of M31 came from spectroscopic studies with the Hectospec multifibre spectrograph (Fabricant et al. 2005) on the 6.5-meter MMT Observatory telescope in Arizona. Using these spectra, Caldwell & Romanowsky (2016) produced metallicity estimates and a collection of uniformly determined line-of-sight velocities for roughly 94% of GCs with projected radii within 21 kpc. During data collection, the metallicities of six inner globular clusters were not measured and were therefore flagged as -99; as a result, we excluded these six GCs. We also decided to remove those GCs with metallicity ≥ -0.4 as these are most likely associated with the disk of M31 (Caldwell & Romanowsky 2016), and also so we would have a dataset consistent with previous research (Lewis et al. 2023). After removing these data points, the metallicity of the remaining inner GCs ranges from $-2.8 < [\text{Fe}/\text{H}] < -0.4$. The inner GC data were obtained through MMT spectroscopy and were originally published by Caldwell & Romanowsky (2016).

The 77 outer GCs, which lack metallicity measurements, have been categorized as either not associated with a substructure (a subgroup of GCs henceforth referred to as GC_{non}), associated with a substructure

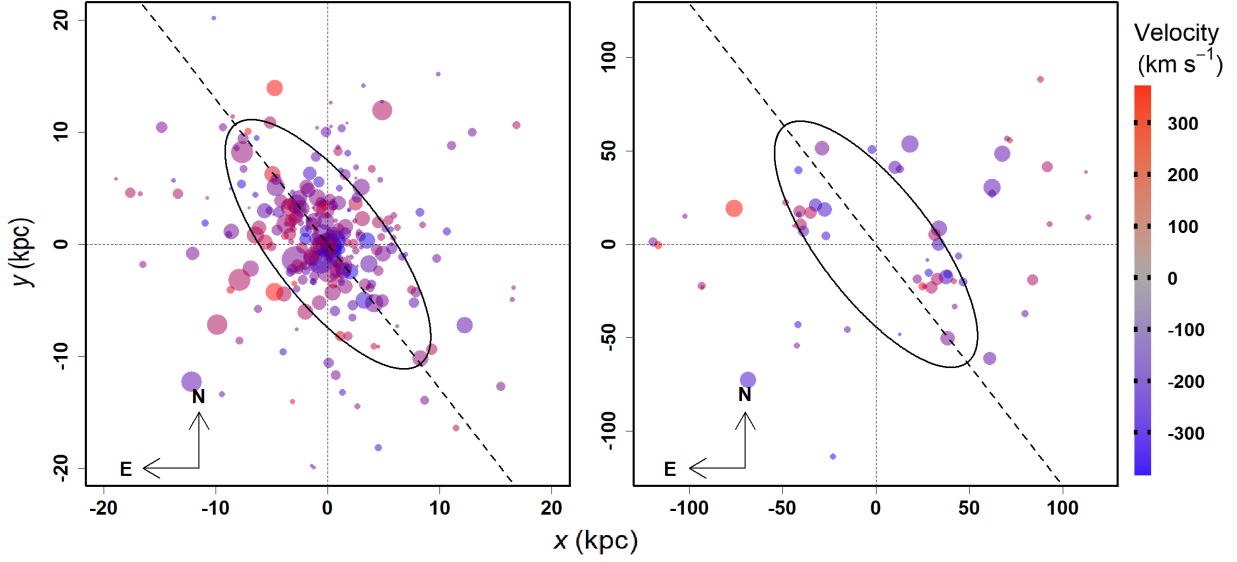


FIG. 2.— Spatial distribution of M31 GCs, studied in this paper, separated into inner ($R_p < 25$ kpc; left panel) and outer ($R_p \geq 25$ kpc; right panel) populations. Points are colored according to line-of-sight velocity relative to the galaxy, with red indicating positive velocities and blue indicating negative velocities. The size of each point is scaled by the absolute value of the velocity. Black ellipses indicate the disk orientation of the M31 galaxy. Compass arrows indicate the north (N) and east (E) directions.

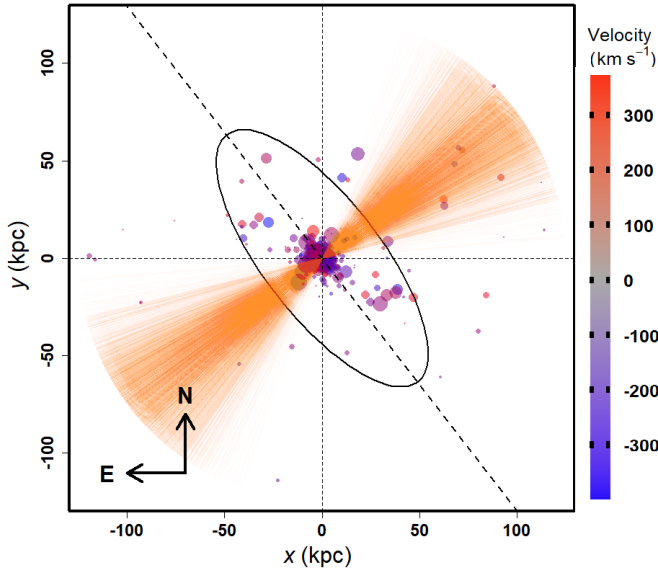


FIG. 3.— The M31 GC population, colour-coded by radial velocity in the M31 frame. The absolute value of the line-of-sight velocity is also indicated by the size of each point. The orange lines are representative samples of the orientation angle drawn from the parameter exploration of Model 1. The ellipse represents M31’s disk orientation.

(henceforth referred to as GC_{sub}), or ambiguous. In Mackey et al. (2019b), the 19 ambiguous clusters were included in the analysis, and an attempt was made to infer their substructure status from the data, based on whether their other properties are more consistent with the GC_{sub} or GC_{non} subpopulations. As our analysis is more complex in other ways (see Section 3), we excluded these ambiguous clusters to limit the complexity of our approach. Hence, in total, 26 GC_{non} and 32 GC_{sub} outer globular clusters were analysed in this study. Note that, due to the complexities of stellar structure in the inner regions of M31, it is not possible to unambiguously associate the inner GCs with distinct stellar substructure. It

should be noted that photometric metallicity estimates are now available (and a few spectroscopic ones) for the outer GCs (McGill et al. 2025); however, we have opted to rely on the complete spectroscopically derived metallicity estimates available for the inner population, as the outer GC metallicities are heterogeneous in origin and not uniformly calibrated. The outer GC data were obtained from PAndAS (McConnachie et al. 2018) and can be downloaded from the Canadian Astronomical Data Center (CADC).

In summary, after combining the datasets from the inner (339) and outer (77) regions, we removed 19 ambiguous outer clusters, six inner clusters without metallicity measurements, and all clusters with metallicity $[\text{Fe}/\text{H}] \geq -0.4$. The final dataset used therefore comprises 336 GCs. The spatial distribution of the inner and outer GCs that we used in this study can be seen in Figure 2.

3. KINEMATIC MODELS AND BAYESIAN INFERENCE

Upon combining the inner and outer GC data, we first investigated the overall rotational orientation of M31’s GCs using a simple kinematic model, which we call Model 1. This model is comprised of only a singular component describing all GCs which serves to capture the overall rotational pattern of the GCs, and to provide a simple baseline for model comparison purposes. The kinematic model employed gives the line-of-sight velocity v as a function of position on the sky (x, y), using the following functional form:

$$v(x, y) = A \sin(\theta - \phi), \quad (1)$$

where (x, y) are the projected coordinates of the GC on the sky, measured relative to the centre of M31, the unknown parameter ϕ indicates the orientation of the GCs’ rotation axis, and A is the amplitude of the rotational velocity. For the implementation of the analysis, ϕ was defined using the mathematical convention with respect to the x and y axes as displayed in Figure 2. For convenience, in the results we present ϕ along with the

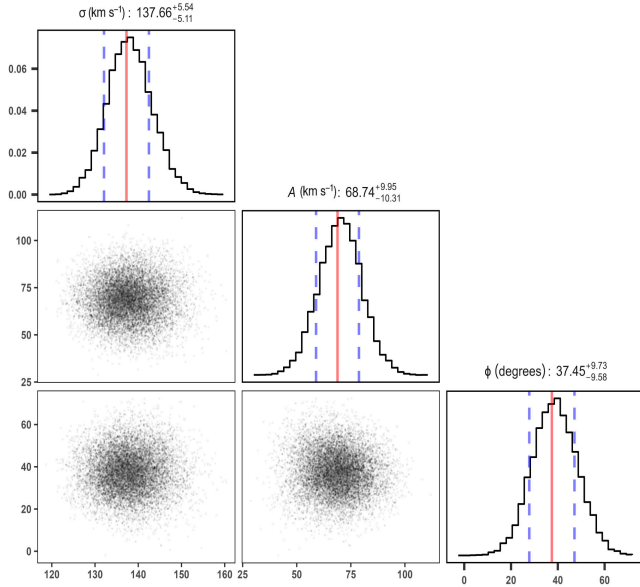


FIG. 4.— Corner plot (Foreman-Mackey 2016) of the posterior distribution for Model 1’s parameters. There are no strong correlations or other dependencies in the posterior distribution, and all of the marginal distributions are normal to a good approximation. The red solid line represents the median (50th percentile), whereas the blue dashed lines indicate the 16th and 84th percentiles of the posterior distribution of the parameters.

standard position angle (PA) defined from north through east.

The quantity θ is the angular coordinate corresponding to (x, y) when translated into plane polar coordinates. We also assume that the single component has a spatially flat velocity dispersion σ , also unknown, which appears in the likelihood function, defined in Section 3.1. Note that the observed line-of-sight velocities are converted to M31-centric velocities. The chosen functional form (Equation 1) is known as the V model, after Veljanoski et al. (2014). However, alternative functional forms are possible. In this study, we also utilized two additional model types, F and S , whose details are given in Appendix A.

3.1. Prior Distributions and the Likelihood Function

Table 1 summarizes the prior distributions for the parameters. In Model 1, there are only three unknown parameters: amplitude A , orientation ϕ , and velocity dispersion σ . It should be noted that while A and ϕ appear explicitly in Equation 1 as part of the line-of-sight velocity model, σ enters the likelihood function (Equation 2) through the variance term, representing the intrinsic velocity dispersion of the GC system.

The velocity dispersion, denoted by σ , quantifies the random motions of the GCs about the modelled systemic rotation. Physically, it reflects the degree to which individual cluster velocities deviate from the mean rotational trend, providing a measure of the dynamical “temperature” or kinematic spread of the system. In the context of our models, σ is included as a parameter in the likelihood function to account for this intrinsic scatter in the observed line-of-sight velocities. A larger σ indicates a more dynamically hot or pressure-supported system, whereas a smaller σ (relative to A) corresponds to a more rotationally supported population.

For simplicity, we have used uniform priors. However,

since we intend to carry out Bayesian model comparison, the limits of the uniform priors need to be considered, as the results will be sensitive to these choices. For the parameters A and σ , we have imposed an upper bound of 1000 km s^{-1} , to rule out astrophysically implausible values. For the orientation angle ϕ , the uniform distribution arises as a natural prior from considerations of rotational symmetry and is automatically bounded.

The probability distribution for the measured line-of-sight velocities v_i given the parameters, which will also form the likelihood function, is assumed to be a normal distribution with mean $v(x_i, y_i)$ and a variance of $\sigma^2 + s_i^2$, where s_i is the reported error bar on velocity i . The likelihood function, assumed to be a normal distribution, is given by

$$\mathcal{L}(A, \phi, \sigma) = \prod_{i=1}^n \frac{1}{\sqrt{2\pi(\sigma^2 + s_i^2)}} \exp\left(-\frac{(v_i - v(x_i, y_i))^2}{2(\sigma^2 + s_i^2)}\right). \quad (2)$$

3.2. Bayesian Inference

Throughout this paper, we calculate posterior distributions for the parameters using Bayesian inference. The posterior distribution for any model parameters ω is obtained by Bayes’s theorem, given by

$$\mathcal{P}(\omega | \mathcal{D}) = \frac{\mathcal{P}(\omega) \mathcal{P}(\mathcal{D} | \omega)}{\mathcal{P}(\mathcal{D})}. \quad (3)$$

Here, ω represents a vector of unknown parameters¹. In Equation 3, \mathcal{D} represents the data, $\mathcal{P}(\omega)$ represents the prior probability distribution of the parameters, $\mathcal{P}(\mathcal{D} | \omega)$ represents the likelihood function, and lastly, $\mathcal{P}(\mathcal{D})$ represents the marginal likelihood value, also known as the evidence.

In this paper, Nested Sampling (Skilling 2004; Ashton et al. 2022) and Diffusive Nested Sampling (Brewer et al. 2011; Brewer & Foreman-Mackey 2018) were used to generate samples from the posterior distribution and to determine the marginal likelihood or evidence of the model, expressed as follows:

$$\mathcal{P}(\mathcal{D}) = \int \mathcal{P}(\omega) \mathcal{P}(\mathcal{D} | \omega) d\omega \quad (4)$$

or alternatively

$$\mathcal{Z} = \int \mathcal{L}(\omega) \pi(\omega) d\omega, \quad (5)$$

where the prior distribution is denoted by $\pi(\omega)$, the likelihood function is denoted by $\mathcal{L}(\omega)$, and the evidence or marginal likelihood is denoted by \mathcal{Z} . Once the marginal likelihoods of the models are determined through nested sampling, we can select the most plausible model based on the highest marginal likelihood value, or we can propagate uncertainty about the model into any final conclusions using probability theory.

Finally, the Bayes Factor, the ratio of the marginal likelihoods of two models, can be determined. It is another way of expressing conclusions which could be expressed as model probabilities. The Bayes Factor describes the

¹ Unknown parameters are traditionally called θ , but this has already been used for the angular coordinate on the sky.

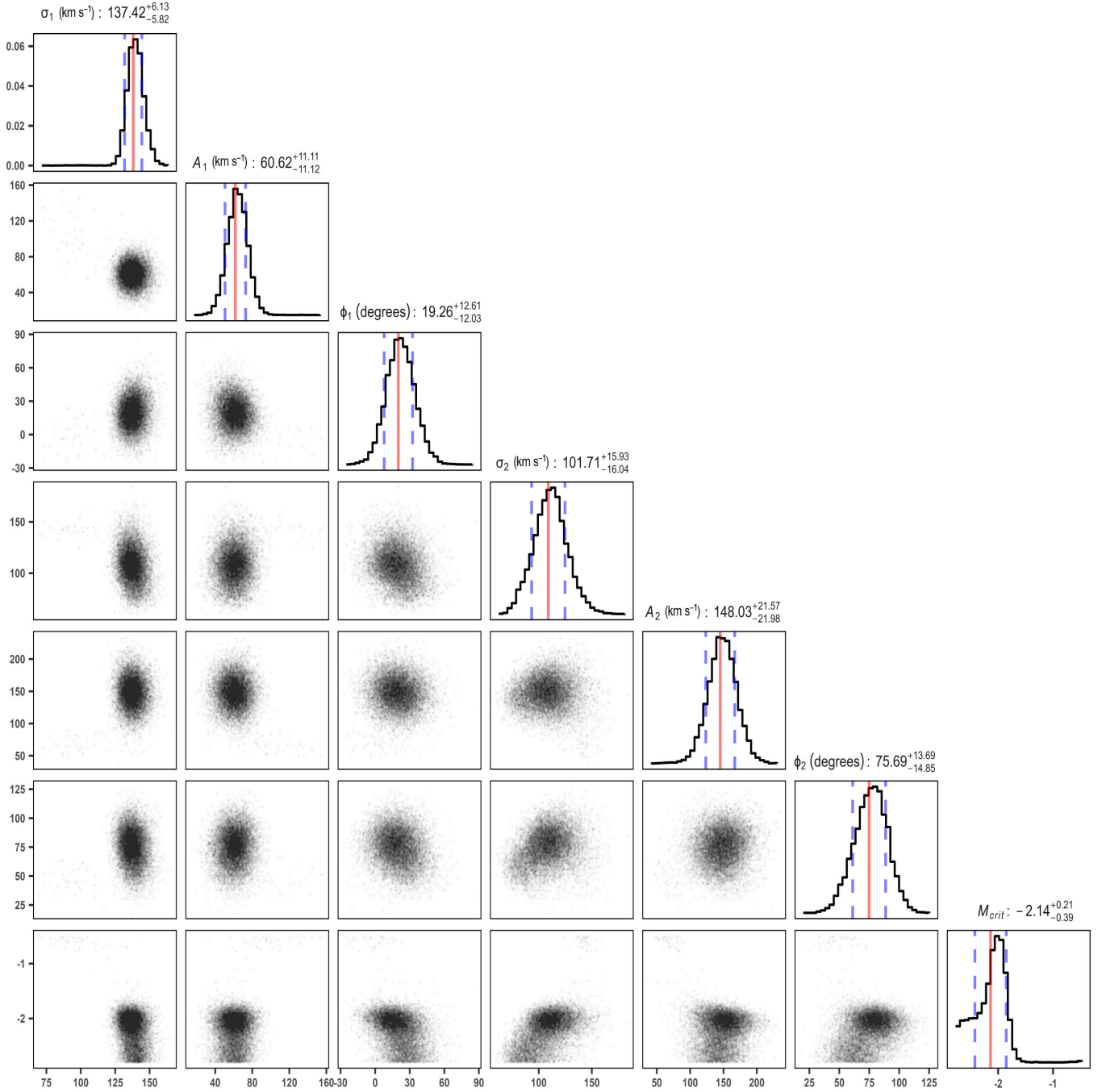


FIG. 5.— The posterior distribution for parameters of Model 2.1. Here, σ_1 , A_1 and ϕ_1 are the components for GC_{non} and higher metallicity GCs, while σ_2 , A_2 and ϕ_2 are the components for GC_{sub} and lower metallicity GCs.

degree to which the data favours one model over the other. The Bayes Factor for comparing some model \mathcal{M}_1 to another \mathcal{M}_2 is represented by the following equation:

$$\mathcal{BF}(\mathcal{M}_1, \mathcal{M}_2) = \frac{\mathcal{P}(\mathcal{D} | \mathcal{M}_1)}{\mathcal{P}(\mathcal{D} | \mathcal{M}_2)}, \quad (6)$$

where \mathcal{M}_i denotes the model.

3.3. Metallicity Uncertainties

Although the models discussed so far do not incorporate metallicity information, other models (described in Section 4) make use of the GCs' metallicities, and there-

fore metallicity uncertainties must be considered. As mentioned in the Section 2, six inner GCs without metallicity measurements and those with metallicity $[\text{Fe}/\text{H}] \geq -0.4$ have been removed; the final sample of inner GCs with measured metallicities comprises 278 objects. Since the uncertainties are provided for the metallicity measurements of the 278 inner GCs, we adopt the same strategy as Lewis et al. (2023). This introduces 278 additional parameters to the model, each representing the unknown “true” metallicity value of an inner GC. The prior distributions for these are assumed to be normal distributions centred on the measured metallicities,

with standard deviations corresponding to uncertainties. When evaluating the likelihood function, for all models in Section 4 except Model 1, which does not incorporate metallicity, the fitted metallicity parameters were used to partition the GC population, rather than the measured metallicity values. For simplicity, we did not employ a hierarchical model, so there is no tendency for one GC's true metallicity value to be informed by another GC's measurement.

4. MODELLING

4.1. Model 1

As discussed above, there are only three unknown parameters in Model 1; amplitude A , orientation ϕ , and velocity dispersion σ . Figure 3 shows sample lines drawn from the posterior distribution to depict the plausible values of the orientation angle ϕ of the rotation on the sky. The orientation angle is estimated to be 37 ± 10 degrees (PA = 307 ± 10 degrees). This is consistent with the direction of Andromeda's stellar disk rotation indicated in Mackey et al. (2019b). According to Figure 4, the posterior distributions of all parameters are approximately Gaussian. Posterior summaries for the parameters are shown in Table 2. The parameter estimates are the posterior median and the 68% central credible interval. The posterior distributions indicate that the velocity dispersion σ is almost certainly greater than the rotational amplitude A . This highlights the complexity of the M31 GC system, as the velocity dispersion acts like a noise term, accounting for deviations from the V model's assumptions about the rotational pattern. Quantitatively, we find $A/\sigma = 0.50^{+0.07}_{-0.08}$, suggesting that the GC system is predominantly dominated by dispersion, with a modest but non-negligible contribution from ordered rotation. The marginal likelihood estimate for this model is $\ln(Z) = -2141.09$, which, as we shall see, is the lowest marginal likelihood of all the models considered.

4.2. Model 2

Model 1, being a simple one-component model, is unlikely to be able to capture all of the complexity of the GC population. Mackey et al. (2019b) found that two rotating components are supported for the outer GCs, where each GC was assigned to one component or the other based on whether it was located on a substructure or not. Similarly, Lewis et al. (2023) split the inner GC population into two components by metallicity, with the metallicity cutoff being a free parameter, also finding evidence for two components. Intriguingly, the orientation angles of one of the components from each study appeared to align. This alignment was between the Duleais structure (observed as lower metallicity inner GCs) and the outer GCs associated with substructures. This motivated us to create a model that unifies the previous two, assigning GCs to components using a rule based on metallicity (for inner GCs) and substructure status (for outer GCs). Using this model, we can formally test the hypothesis that the Duleais structure and the GC_{sub} outer population share the same rotational characteristics, and potentially the same origin. As in previous studies, we introduce a critical metallicity value, M_{crit} , as a free parameter to determine how each GC from the inner population is assigned to one rotational

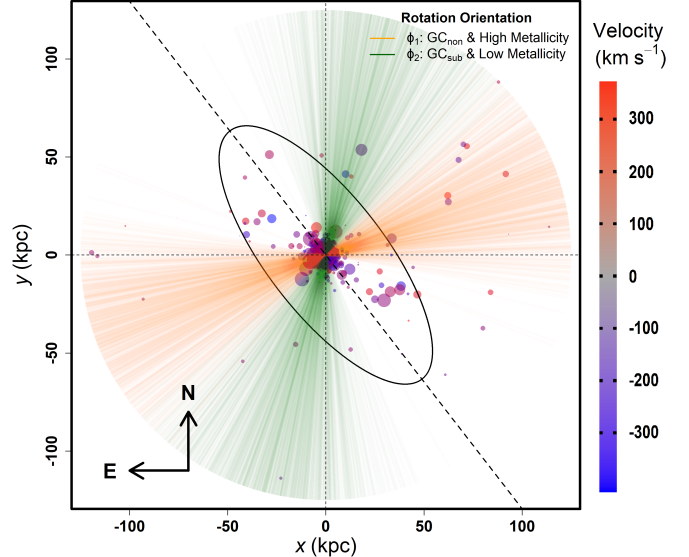


FIG. 6.— As Figure 3, but for Model 2.1. Here, the GC_{sub} and the lower metallicity GCs are grouped together under component 2, with the green lines representing the orientation of the rotational axis drawn from the posterior distribution. The orientation of component 2 agrees with that found in Lewis et al. (2023, see Figure 2), who first suggested the potential association between these two populations.

TABLE 3
RULES FOR ASSIGNING EACH GC TO ONE ROTATING COMPONENT
OR THE OTHER; MODELS 2.1 AND 2.2.

Model	Conditions	Parameters
Model 2.1	GC _{non} or Metallicity > M_{crit} GC _{sub} or Metallicity $\leq M_{\text{crit}}$	A_1, ϕ_1 , and σ_1 A_2, ϕ_2 , and σ_2
Model 2.2	GC _{sub} or Metallicity > M_{crit} GC _{non} or Metallicity $\leq M_{\text{crit}}$	A_1, ϕ_1 , and σ_1 A_2, ϕ_2 , and σ_2

component or the other. The prior for M_{crit} is taken to be Uniform($-2.8, -0.5$), encompassing the full range of measured inner GC metallicities. This range is chosen because, after excluding GCs with metallicities ≥ -0.4 , the highest remaining metallicity is -0.5 , so the range ($-2.8, -0.5$) covers the whole range of the metallicity values used in the analysis. This framework allows us to perform model selection to test different rules for assigning individual GCs to one rotational component or the other. In terms of regression models, we are attempting to explain the response variable (radial velocity) in terms of GC position, along with metallicity and/or substructure status as the explanatory variables. With the metallicity cut, the model suddenly changes behaviour as a function of the explanatory variables. Therefore, this model can be considered to be a change-point model.

In two-component models, the line-of-sight velocity v as a function of position for each component $j \in \{1, 2\}$ is given by

$$v_j(x, y) = A_j \sin(\theta - \phi_j). \quad (7)$$

Each component has its own rotational amplitude A_j and orientation angle ϕ_j , along with its own velocity dispersion σ_j (c.f. Equation 2). The selection of the appropriate component for each GC is made based on the GC's properties such as its metallicity (for inner GCs) or its substructure status (for outer GCs).

TABLE 4
SUMMARY TABLE OF MODEL 2.1'S PARAMETER ESTIMATES.

Components	Parameters	Estimates
Rotational Component 1	σ_1 (km s ⁻¹)	137.42 ^{+6.13} _{-5.82}
	A_1 (km s ⁻¹)	60.62 ^{+11.11} _{-11.12}
	ϕ_1 (degrees)	19.26 ^{+12.61} _{-12.06}
	PA ₁ (degrees)	289.26 ^{+12.61} _{-12.06}
	A_1/σ_1 ratio	0.44 ^{+0.08} _{-0.08}
Rotational Component 2	σ_2 (km s ⁻¹)	101.71 ^{+15.93} _{-16.04}
	A_2 (km s ⁻¹)	148.03 ^{+21.57} _{-21.98}
	ϕ_2 (degrees)	76.69 ^{+13.69} _{-14.85}
	PA ₂ (degrees)	346.69 ^{+13.69} _{-14.85}
	A_2/σ_2 ratio	1.39 ^{+0.30} _{-0.27}
M_{crit}		-2.14 ^{+0.21} _{-0.39}

Under a two-component model, we must divide the overall GC population into two subpopulations. There are two different ways to do this, which we call Models 2.1 and 2.2 (Table 3). Model 2.1 is motivated by the observation of Lewis et al. (2023) that the lower metallicity inner GCs and the GC_{sub} outer GCs appear to share the same orientation. Therefore, Model 2.1 assumes a GC belongs to rotational component 1 if it is GC_{non} or has metallicity above M_{crit} ; otherwise, it belongs to rotational component 2 (GC_{sub} and metallicity $\leq M_{\text{crit}}$ clusters).

To determine whether the data indeed support this expectation, we also considered an alternative assumption for the two-component model, which we call Model 2.2. This model uses swaps the way the GCs are grouped; that is, if a GC is a GC_{sub} or higher metallicity GC, it belongs to rotational component 1, otherwise (i.e. if it is a GC_{non} or lower metallicity GC) it belongs to rotational component 2. These assignment rules are the opposite of those in Model 2.1. The reasoning behind these ideas is that if galaxies were accreted onto M31 at different epochs, each of these galaxies would bring its own population of globular clusters. As a result, the GC population in M31 would be separated into various subgroups with different kinematic features. If there is truly an association between the Dulais structure (inner lower metallicity GCs) and the outer GC_{sub} clusters, we should expect to see Model 2.1 outperform Model 2.2.

4.2.1. Model 2.1 Results

Under this assumption, GC_{non} and higher metallicity GCs are grouped together using the parameters A_1 , ϕ_1 , and σ_1 , while GC_{sub} and lower metallicity clusters share a common rotational component characterized by A_2 , ϕ_2 , and σ_2 . Figure 5 illustrates the posterior distributions of the parameters for Model 2.1. Most of the posterior probability for M_{crit} is below -1.8 with most of the probability centered around -2.14, while all other parameters have fairly symmetric posterior distributions. There are 278 inner GCs of M31 with a metallicity value above -2.14 and only 9 inner GCs with a metallicity value less than or equal to -2.14 — the proportion of the population with metallicity below M_{crit} is small. Figure 6

TABLE 5
PARAMETER ESTIMATES FOR MODEL 2.2.

Components	Parameter	Estimate
Rotational Component 1	σ_1 (km s ⁻¹)	92.23 ^{+14.64} _{-11.36}
	A_1 (km s ⁻¹)	132.19 ^{+21.61} _{-18.87}
	ϕ_1 (degrees)	56.36 ^{+11.28} _{-10.43}
	PA ₁ (degrees)	326.36 ^{+11.28} _{-10.43}
	A_1/σ_1 ratio	1.45 ^{+0.31} _{-0.34}
Rotational Component 2	σ_2 (km s ⁻¹)	143.02 ^{+6.76} _{-6.99}
	A_2 (km s ⁻¹)	55.77 ^{+13.59} _{-12.68}
	ϕ_2 (degrees)	-21.18 ^{+14.49} _{-15.23}
	PA ₂ (degrees)	248.82 ^{+14.49} _{-15.23}
	A_2/σ_2 ratio	0.39 ^{+0.10} _{-0.09}
M_{crit}		-0.58 ^{+0.05} _{-0.11}

demonstrates that the rotational angle, ϕ_1 (shown with orange lines), for the GC_{non} and high metallicity GCs is 19 ± 12 degrees (PA = 289 ± 12 degrees), while the average rotational angle, ϕ_2 (the green lines), for GC_{sub} and lower metallicity GCs is 108 ± 16 degrees (PA = 18 ± 16 degrees). Lastly, Table 4 shows the posterior summaries for the parameters. The posterior median of A_2 (the rotation velocity of lower metallicity and GC_{sub} clusters) is higher than A_1 (higher metallicity and GC_{non} clusters). The A_j/σ_j (or equivalently V/σ) ratio is calculated for each rotational component that quantifies the balance between ordered rotation (V) and random motion (σ). Systems with higher A/σ values are rotation-dominated, whereas those with lower A/σ values are dispersion-dominated. Under this assumption, the corresponding kinematic ratios are $A_1/\sigma_1 = 0.44^{+0.08}_{-0.08}$ for the first component and $A_2/\sigma_2 = 1.39^{+0.30}_{-0.27}$ for the second, indicating that the GC_{non} and higher metallicity GC population is predominantly dominated by dispersion, whereas the GC_{sub} and lower metallicity GC population is largely rotation-dominated. The marginal likelihood estimate of Model 2.1 is $\ln(Z) = -2139.40$, which is the highest marginal likelihood of all the models considered.

4.2.2. Model 2.2 Results

Model 2.2 is the two-component model, but with different assumptions about which subpopulation of inner GCs is associated with which subpopulation of the outer GCs. For this assumption, GC_{sub} and higher metallicity GCs are grouped together with parameters A_1 , ϕ_1 , and σ_1 . Conversely, GC_{non} and lower metallicity GCs share a common rotational component using A_2 , ϕ_2 , and σ_2 . This grouping is the opposite of that suggested by Lewis et al. (2023), who found that lower metallicity inner GCs (the Dulais structure) are more plausibly associated with the outer GC_{sub} population.

Figure 7 shows the posterior distributions for the parameters of Model 2.2. The posterior distribution for M_{crit} is bimodal with most of the probability centred around -0.58, in this case the second mode contains only a very small amount of probability. The posterior distribution for σ_1 and σ_2 seems to be bimodal, again with the second mode containing only a very small amount

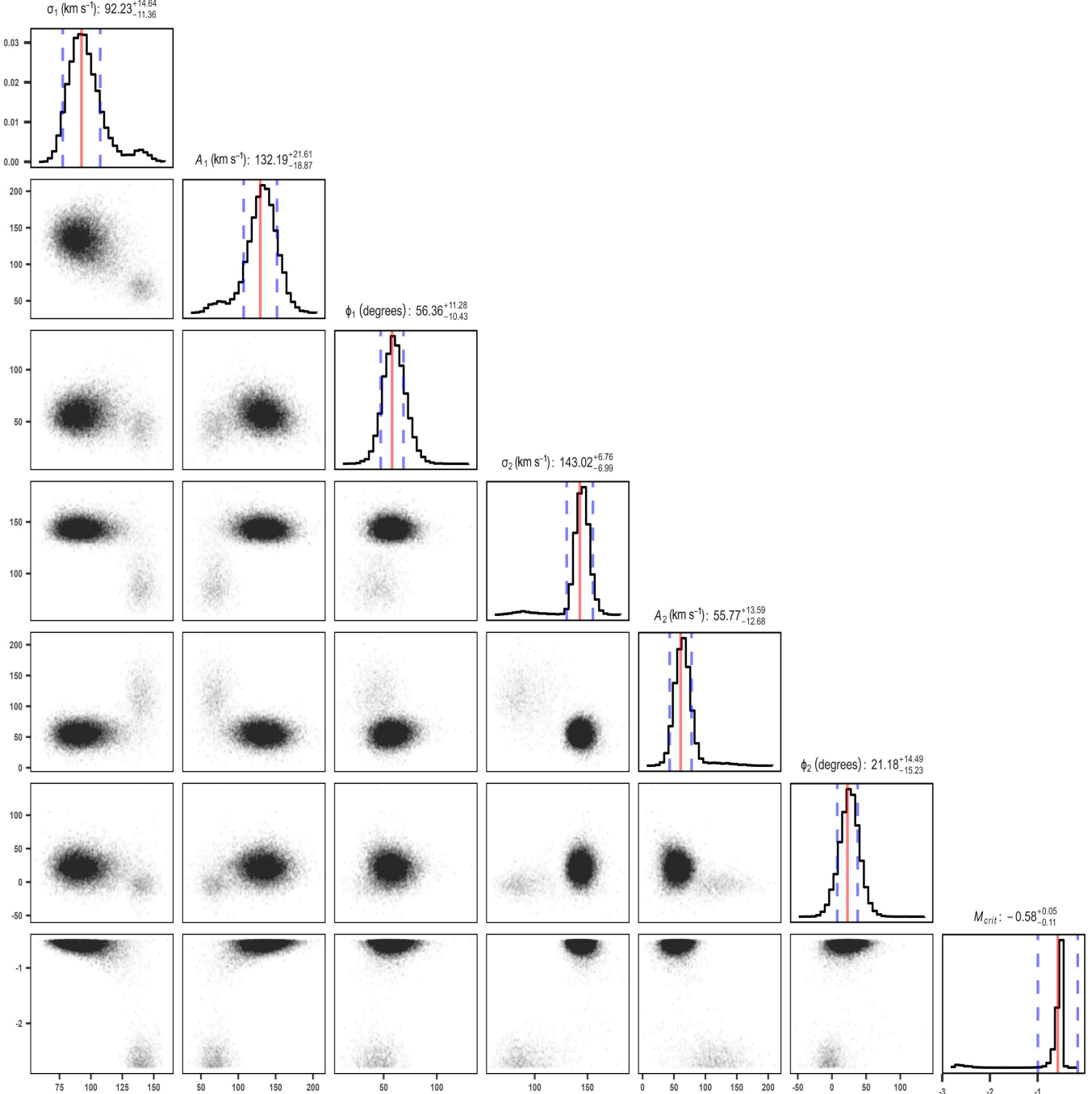


FIG. 7.— Posterior distribution for parameters of Model 2.2. Here, σ_1 , A_1 and ϕ_1 are the parameters for GC_{sub} and higher metallicity GCs, while σ_2 , A_2 and ϕ_2 are the parameters for GC_{non} and lower metallicity GCs.

of probability. For all other parameters the posterior distributions are reasonably symmetric. Figure 8 shows posterior samples for the orientation of rotation for the two components. This shows that, under the assumption that the higher metallicity GCs and GC_{sub} share a common rotation axis, their orientation angle ϕ_1 is 56^{+11}_{-10} degrees (PA = 326^{+11}_{-10} degrees). This angle agrees with the orientation of Andromeda’s stellar disk from the previous studies (Mackey et al. 2019b). Conversely, ϕ_2 (the green lines) reveals that, under the assumption that the lower metallicity GCs and GC_{non} share a similar rotation

axis, their rotational orientation ϕ_2 is -21 ± 15 degrees (PA = 249 ± 15 degrees). Lastly, Table 5 displays the posterior summary statistics for the parameters. Quantitatively, the kinematic ratios are $A_1/\sigma_1 = 1.45^{+0.31}_{-0.34}$ for the first component and $A_2/\sigma_2 = 0.39^{+0.10}_{-0.09}$ for the second. These values indicate that the component associated with the higher metallicity and GC_{sub} clusters is rotation-dominated, whereas the component linked to the lower metallicity and GC_{non} clusters is primarily dispersion-supported. Moreover, the marginal likelihood estimate for this scenario is $\ln(Z) = -2141.78$, which is

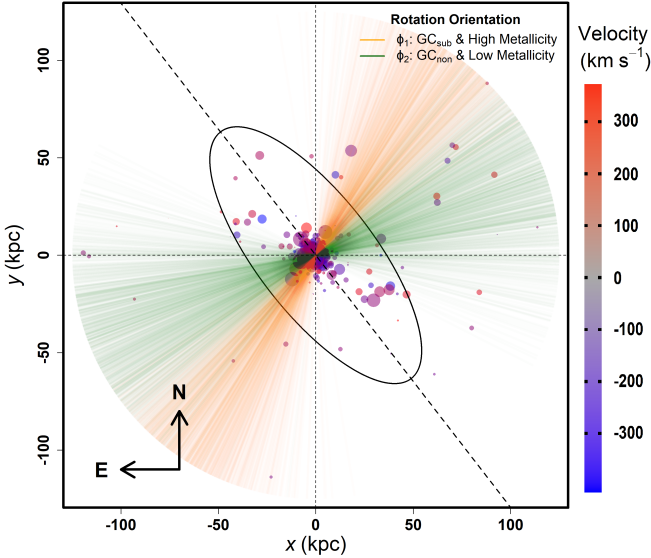


FIG. 8.— As Figure 3, but for Model 2.2. This assigns GC_{sub} and higher metallicity GCs to one component and GC_{non} or lower metallicity GCs to the other. The orientations are significantly different than for Model 2.1; however, Model 2.2 is less preferred than Model 2.1.

below those of Models 1 and 2.1.

4.2.3. Interpretation of the Posterior Distributions for M_{crit}

The posterior distributions of M_{crit} shown in Figures 5 and 7, for Models 2.1 and 2.2 respectively, exhibit markedly different features due to the distinct rules each model uses to assign GCs to rotational components (Table 3). In Model 2.1, the proposed association between inner and outer GCs is physically motivated as the previous findings from Lewis et al. (2023) suggest a kinematic connection between the lower metallicity inner population and the outer GC_{sub} clusters. As a result, the posterior distribution of M_{crit} in Model 2.1 is centred around -2.14 , effectively separating a small (size ~ 10) low-metallicity subset of clusters from the rest.

In contrast, Model 2.2 assigns higher metallicity clusters and GC_{sub} clusters to one component, and lower metallicity and GC_{non} clusters to the other. This is less physically motivated, as there is little previous evidence that GC_{non} outer clusters share a common origin with the lower metallicity inner clusters. The posterior for M_{crit} under Model 2.2 is bimodal with the most significant peak close to -0.6 . This cutoff includes a much larger fraction of inner GCs in the low metallicity group, effectively reclassifying many GCs with moderate metallicity into the same kinematic component as the GC_{non} outer population.

4.3. Model 3

Finally, a three-component model, Model 3, was also considered. In Model 2.1, we considered the potential association between the Dulais structure and the GC_{sub} outer clusters. All other GCs were assigned to the other component. However, it is possible that the connection between GC_{sub} outer clusters and lower-metallicity inner GCs suggested by Lewis et al. (2023) exists, yet there is no association between the higher metallicity inner clusters and the GC_{non} outer ones. Therefore, in Model 3, we assume that the population is split

TABLE 6
RULES FOR ASSIGNING GCs TO SUBGROUPS FOR MODEL 3.

Conditions	Rotating Components
$Metallicity > M_{crit}$	A_1, ϕ_1 , and σ_1
GC_{non}	A_2, ϕ_2 , and σ_2
GC_{sub} or Metallicity $\leq M_{crit}$	A_3, ϕ_3 , and σ_3

TABLE 7
PARAMETER ESTIMATES FOR MODEL 3.

Components	Parameters	Estimates
Rotational Component 1	σ_1 (km s $^{-1}$)	$141.49^{+6.62}_{-6.21}$
	A_1 (km s $^{-1}$)	$57.36^{+11.78}_{-11.37}$
	ϕ_1 (degrees)	$26.74^{+14.74}_{-14.73}$
	PA_1 (degrees)	$296.74^{+14.74}_{-14.73}$
	A_1/σ_1 ratio	$0.41^{+0.08}_{-0.09}$
Rotational Component 2	σ_2 (km s $^{-1}$)	$88.13^{+15.78}_{-11.71}$
	A_2 (km s $^{-1}$)	$123.11^{+28.58}_{-30.46}$
	ϕ_2 (degrees)	$-4.09^{+10.62}_{-10.58}$
	PA_2 (degrees)	$265.91^{+10.62}_{-10.58}$
	A_2/σ_2 ratio	$1.40^{+0.40}_{-0.41}$
Rotational Component 3	σ_3 (km s $^{-1}$)	$104.03^{+16.83}_{-16.94}$
	A_3 (km s $^{-1}$)	$146.72^{+21.03}_{-21.46}$
	ϕ_3 (degrees)	$72^{+14.65}_{-15.12}$
	PA_3 (degrees)	$342^{+14.65}_{-15.12}$
	A_3/σ_3 ratio	$1.42^{+0.31}_{-0.28}$
	M_{crit}	$-2.23^{+0.26}_{-0.39}$

into three groups: higher metallicity GCs from the inner population are assigned to the first component. A GC_{non} from the outer clusters is assigned to the second component. Finally, the lower metallicity inner GCs and the GC_{sub} outer GCs are assigned to the third component (Table 6). This grouping is physically motivated, as previous studies (Lewis et al. 2023) suggest a connection between GC_{sub} outer GCs and low-metallicity populations. This final component is the same as in Model 2.1 and is the one highlighted throughout this paper.

For the three-component model, the line-of-sight velocity v as a function of position for each component $j \in \{1, 2, 3\}$ has a form given by Equation 7. Each of the three components has its own rotational amplitude A_j , orientation angle ϕ_j , and velocity dispersion σ_j . As with the previous models, the velocity dispersion contributes to the variance term in the likelihood function.

Figure 9 illustrates that the posterior samples of M_{crit} are below $[Fe/H] = -1.7$, with most of the possibilities centered around $[Fe/H] = -2.23$ (in agreement with Model 2.1), while all other parameters have approximately normal posterior distributions. Figure 10 illustrates that the average rotating angle ϕ_1 (the orange lines) for the higher metallicity inner GCs, is 27 ± 15 degrees ($PA = 297 \pm 15$ degrees). The orientation angle ϕ_2 (the green lines), for the GC_{non} is -4 ± 11 degrees ($PA = 266 \pm 11$ degrees), and ϕ_3 (the purple lines) for the GC_{sub} and lower-metallicity GCs is 72 ± 15 de-

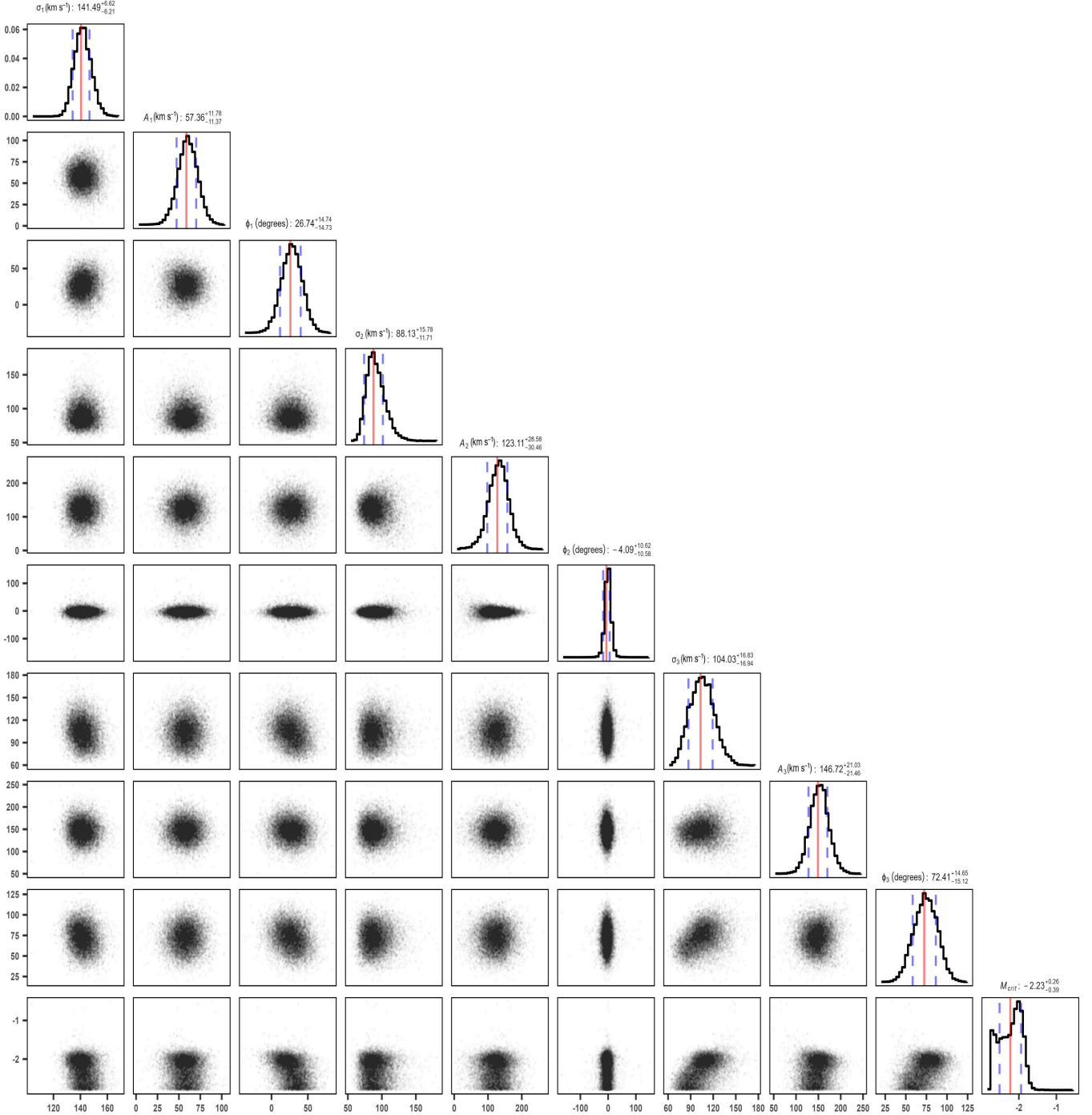


FIG. 9.— Posterior distributions for Model 3. Parameters σ_1 , A_1 , and ϕ_1 correspond to the higher-metallicity inner GCs; σ_2 , A_2 , and ϕ_2 to the GC_{non} outer clusters; and σ_3 , A_3 , and ϕ_3 to the GC_{sub} and lower-metallicity GCs.

grees (PA = 342 ± 15 degrees). This latter result is consistent with the conclusion of Model 2.1. Interestingly, the higher metallicity inner GCs in Model 3 rotate in the same direction as M31's stellar disk, consistent with previous findings (Mackey et al. 2019b). Quantitatively, the kinematic ratios are $A_1/\sigma_1 = 0.41^{+0.08}_{-0.09}$ for the first component, $A_2/\sigma_2 = 1.40^{+0.40}_{-0.41}$ for the second, and $A_3/\sigma_3 = 1.42^{+0.31}_{-0.28}$ for the third. These results indicate that the higher metallicity inner GCs (component 1) are primarily dispersion supported, whereas both the GC_{non}

(component 2) and the GC_{sub} together with lower metallicity GCs (component 3) exhibit rotation dominated kinematics. The posterior summaries for the parameters are shown in Table 7. The marginal likelihood estimate for Model 3 is $\ln(Z) = -2141.03$, which is the second highest of the four models considered in this paper, behind Model 2.1.

4.4. Bayesian evidence comparison

The marginal likelihoods (evidence) for the models are given in Table 8, along with the Bayes Factors relative

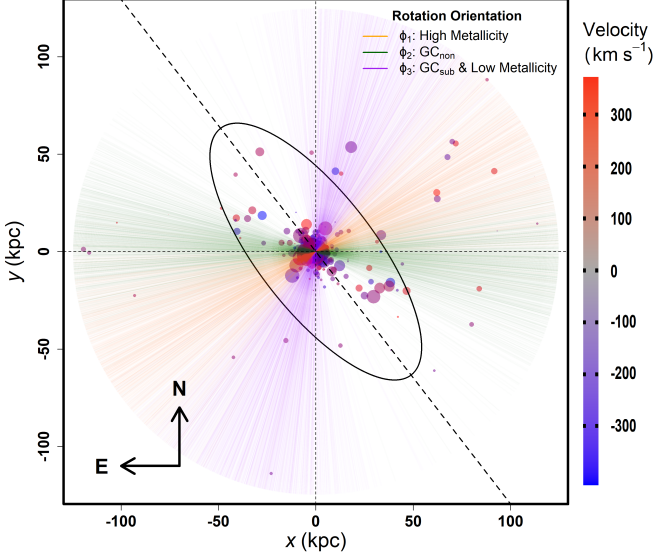


FIG. 10.— As Figure 3 but for Model 3. This assigns higher metallicity inner GCs component 1, GC_{non} to component 2, and GC_{sub} or lower metallicity GCs to component 3. The angle of orientation of component 3 agrees with the equivalent component of Model 2.1. The model comparison calculation suggests this model is the second-best model behind Model 2.1.

to the best model (Model 2.1). The following equation provides an example of determining the Bayes Factor, in this case for Model 2.1 versus Model 2.2:

Bayes Factor =

$$\begin{aligned}
 \frac{Z_{2.1}}{Z_{2.2}} &= \exp(\log \mathcal{P}(\mathcal{D} | \mathcal{M}_{2.1}) - \log \mathcal{P}(\mathcal{D} | \mathcal{M}_{2.2})) \\
 &= \exp(-2139.40 - (-2141.78)) \\
 &\approx 11.
 \end{aligned} \tag{8}$$

Following Kass & Raftery (1995), a Bayes Factor ranging from 3.2 to 10 indicates substantial evidence in favour of one model over another, and strong evidence is indicated by a Bayes factor between 10 and 100. Based on this, Bayes Factors of approximately 5, 11, and 6 for Model 2.1 versus the alternatives indicate that the data provide substantial to strong support for Model 2.1. The Bayes Factor further indicates that the alternative assumption for the two-component model (Model 2.2), indeed, is not a plausible model. Table 8 shows the evidence ratios relative to Model 2.1, this time with the ratio inverted so that the Bayes Factors are less than one. Moreover, if the prior probabilities of each of the four models are all equal to 1/4, the posterior probabilities become (0.12, 0.68, 0.06, 0.13) respectively. There is significant plausibility for Model 2.1 and some plausibility for Model 3, whose implications are similar to Model 2.1, in that they both assume the association suggested by Lewis et al. (2023). Model 1, while disfavoured by the data, is not completely ruled out.

5. DISCUSSION AND CONCLUSIONS

Here, we have explored various hypotheses about the kinematic structure of M31’s GC population. Motivated primarily by previous separate studies of the inner (Lewis et al. 2023) and outer (Mackey et al. 2019b) GC populations, we have combined the two populations and per-

TABLE 8
THE MARGINAL LIKELIHOOD ESTIMATES FOR EACH OF THE FOUR MODELS CONSIDERED IN THIS PAPER.

Model	$\ln Z$	Z/Z_{\max}
Model 1	-2141.09	0.18
Model 2.1	-2139.40	1.00
Model 2.2	-2141.78	0.09
Model 3	-2141.03	0.20

formed a unified analysis. Since the evidence supports two distinct subpopulations for both the inner and outer GCs when analysed separately, we investigated the possibility that one of the inner subpopulations is associated with one of the outer subpopulations, which could occur as a result of being accreted onto M31 as part of one accretion event. It should be noted that, as mentioned in Section 2, photometric metallicity estimates (and a few spectroscopic ones) are now available for the outer GCs (McGill et al. 2025). However, due to the heterogeneous origin and incomplete coverage of the outer GC sample, these metallicities were not included in the modelling process.

Model 1 (Subsection 4.1) provides a baseline, showing that the overall rotation axis of the GC population aligns with Andromeda’s stellar disk. However, this model is not well supported in the final model comparison. In Models 2.1 and 2.2, we divide the GCs into two components, by metallicity for inner GCs and by substructure association for outer GCs, to test different assumptions about their shared origins. These models explore whether inner and outer GCs could have been deposited by the same progenitor galaxies during separate accretion events. Following Lewis et al. (2023), Model 2.1 assumes that lower-metallicity inner GCs and substructure-associated outer GCs form a single population. This hypothesis is strongly supported by the data and predicts a rotation axis that is nearly north-south on the sky, consistent with previous findings (see Figure 6). In contrast, Model 2.2, which assumes the opposite association, is disfavoured. Table 4 (for Model 2.1) shows that the posterior for amplitude $A_1 \sim 50 - 70 \text{ km s}^{-1}$, is significantly lower than for A_2 with a velocity of $\sim 125 - 170 \text{ km s}^{-1}$, implying that the lower-metallicity or substructure GCs rotate about 2.4 times faster than their higher-metallicity or non-substructure counterparts. It appears that the lower-metallicity or substructure GCs rotate faster but also have a lower velocity dispersion. Considering the velocity dispersion (see Table 4), the corresponding kinematic ratios are $A_1/\sigma_1 = 0.44^{+0.08}_{-0.08}$ for the higher-metallicity or non-substructure GCs and $A_2/\sigma_2 = 1.39^{+0.30}_{-0.27}$ for the lower-metallicity or substructure GCs. This indicates that the higher-metallicity or non-substructure GCs are predominantly dispersion supported, whereas the lower-metallicity or substructure GCs are largely rotation dominated. Note that this comparison excludes GCs not studied in this paper — those with metallicities greater than or equal to -0.4 — which exhibit coherent rotation aligned with the stellar disk. The stronger coherent rotation of the lower-metallicity and substructure GCs may reflect the accretion history of M31, where these clusters, (possibly due to having been accreted more recently), retain angular momentum from their progenitor systems,

while higher-metallicity clusters have been dynamically heated and partially isotropized.

Finally, a three-component model (Model 3) was also explored to further examine the relationships between the different GC subgroups. This model, which seeks to identify further substructures within the GC population, whilst not as strongly supported as Model 2.1, is the second most plausible model considered. Additionally, the result from Model 3 demonstrates that the higher metallicity inner clusters rotate in the same direction as Andromeda’s stellar disk, consistent with previous studies (Mackey et al. 2019b). The physical implications of Model 3 and Model 2.1, the two best-supported models, are similar, and both support the proposed association of Lewis et al. (2023). The existence of metallicity estimates for a subset of the outer GCs raises the question of whether there is a metallicity difference between the GC_{sub} and GC_{non} outer populations. A naive extrapolation of our results might suggest that the GC_{sub} population should typically have lower metallicity. McGill et al. (2025) stated that they did not detect any substantial metallicity difference between these two populations. However, their Figure 3 suggests that there might indeed be slightly more low-metallicity GCs in the substructure group. Testing this possibility formally would require in-

corporating these additional measurements into the analysis would require significant and complex changes to the models.

As a closing remark, these results highlight the complexity of M31’s accretion history, revealing that its GC system comprises dynamically and chemically distinct subpopulations likely deposited during multiple accretion events. To further unravel this history, more metallicity measurements in the outer halo are essential, particularly to clarify the nature and extent of structures like the Dulais. Additionally, accurate distance estimates are needed to reconstruct the full three-dimensional spatial distribution of clusters, as the Dulais Structure is likely to lie along the line of sight to the central regions of M31. Hence, future photometry and spectroscopy of the GC populations will be essential in unravelling the accretion history of Andromeda.

ACKNOWLEDGMENTS

We are grateful to Annette M. N. Ferguson (Edinburgh) and Daniel Zucker (Macquarie) for insight on earlier versions of this work and comments that improved the presentation of the results. We also thank the two anonymous referees and the editor who provided useful feedback.

REFERENCES

Akib I., Hammer F., Yang Y., Pawlowski M. S., Wang J., 2025a, *A&A*, 694, A66

Akib I., Hammer F., Yang Y., 2025b, *A&A*, 695, L5

Ashton G., et al., 2022, *Nature Reviews Methods Primers*, 2, 39

Barmby P., Huchra J. P., 2001, *AJ*, 122, 2458

Beasley M. A., 2020, in , *Reviews in Frontiers of Modern Astrophysics; From Space Debris to Cosmology*. pp 245–277, doi:10.1007/978-3-030-38509-5_9

Beasley M. A., Brodie J. P., Strader J., Forbes D. A., Proctor R. N., Barmby P., Huchra J. P., 2004, *AJ*, 128, 1623

Brewer B., Foreman-Mackey D., 2018, *Journal of Statistical Software, Articles*, 86, 1

Brewer B. J., Pártay L. B., Csányi G., 2011, *Statistics and Computing*, 21, 649

Burstein D., et al., 2004, *ApJ*, 614, 158

Caldwell N., Romanowsky A. J., 2016, *ApJ*, 824, 42

Carignan C., Chemin L., Huchmeier W. K., Lockman F. J., 2006, *ApJ*, 641, L109

Côté P., et al., 2001, *ApJ*, 559, 828

Crampton D., Cowley A. P., Schade D., Chayer P., 1985, *ApJ*, 288, 494

Elson R. A., Walterbos R. A. M., 1988, *ApJ*, 333, 594

Fabricant D., et al., 2005, *PASP*, 117, 1411

Forbes D. A., et al., 2018, *Proceedings of the Royal Society of London Series A*, 474, 20170616

Foreman-Mackey D., 2016, *The Journal of Open Source Software*, 1, 24

Harris W. E., Harris G. L. H., Alessi M., 2013, *ApJ*, 772, 82

Ibata R., Martin N. F., Irwin M., Chapman S., Ferguson A. M. N., Lewis G. F., McConnachie A. W., 2007, *ApJ*, 671, 1591

Johnston K. V., Bullock J. S., Sharma S., Font A., Robertson B. E., Leitner S. N., 2008, *ApJ*, 689, 936

Kass R. E., Raftery A. E., 1995, *Journal of the American Statistical Association*, 90, 773

Kavelaars J. J., Hanes D. A., 1997, *MNRAS*, 285, L31

Lewis G. F., Brewer B. J., Mackey D., Ferguson A. M. N., Li Y. C., Adams T., 2023, *MNRAS*, 518, 5778

Mackey A. D., et al., 2007, *ApJ*, 655, L85

Mackey A. D., et al., 2010, *ApJ*, 717, L11

Mackey D., Huxor A., Ferguson A., 2012, in {W. Aoki, M. Ishigaki, T. Suda, T. Tsujimoto, N. Arimoto} ed., *Galactic Archaeology: Near-Field Cosmology and the Formation of the Milky Way*. Astronomical Society of the Pacific, pp 275–278pp, <https://aspbooks.org/publications/458/275.pdf>

Mackey A. D., et al., 2019a, *MNRAS*, 484, 1756

Mackey D., et al., 2019b, *Nature*, 574, 69

McConnachie A. W., et al., 2009, *Nature*, 461, 66

McConnachie A. W., et al., 2018, *ApJ*, 868, 55

McGill G., et al., 2025, *MNRAS*, 542, L60

Peñarrubia J., Ma Y.-Z., Walker M. G., McConnachie A., 2014, *MNRAS*, 443, 2204

Riess A. G., Fliri J., Valls-Gabaud D., 2012, *ApJ*, 745, 156

Schiavon R. P., Caldwell N., Morrison H., Harding P., Courteau S., MacArthur L. A., Graves G. J., 2012, *AJ*, 143, 14

Skilling J., 2004, in Fischer R., Preuss R., Toussaint U. V., eds, *American Institute of Physics Conference Series Vol. 735, Bayesian Inference and Maximum Entropy Methods in Science and Engineering: 24th International Workshop on Bayesian Inference and Maximum Entropy Methods in Science and Engineering*. pp 395–405, doi:10.1063/1.1835238

Veljanoski J., et al., 2014, *MNRAS*, 442, 2929

APPENDIX

APPENDIX A: OTHER KINEMATIC MODELS

In this study, we analysed the data under the assumption of the V model, a specific functional form for the radial velocity as a function of position on the sky. Here, we enlarge the set of possible functions by considering an S (solid body) and F (asymptotically flat) model as well. The functional form of each rotational model is displayed in Table 9, and below is the description of each model:

TABLE 9
LINE-OF-SIGHT VELOCITY OF MODELS V , S , AND F .

Model	Functional form
V	$v_r(x_i, y_i) = A \sin(\theta_i - \phi)$
S	$v_r(x_i, y_i) = A(x_i \sin(\phi) - y_i \cos(\phi))$
F	$v_r(x_i, y_i) = A \tanh((x_i \sin(\phi) - y_i \cos(\phi))/L)$

TABLE 10
MARGINAL LIKELIHOOD $\ln Z$ ESTIMATES FOR THE THREE KINEMATIC MODELS.

Model	Model 1	Model 2.1	Model 2.2	Model 3
V	-2140.09	-2139.40	-2141.78	-2141.03
S	-2154.63	-2161.22	-2161.05	-2165.38
F	-2139.83	-2138.23	-2141.23	-2141.53

- Model V was presented by Côté et al. (2001) as well as Veljanoski et al. (2014). This model considers a line-of-sight velocity profile that varies smoothly as a function of angle. This model was assumed throughout the main part of the paper.
- Model S denotes a solid-body rotation of the GC population, in which the velocity grows linearly with distance from the rotation axis.
- Model F represents an asymptotically flat rotation of the GC population. It assumes that line-of-sight velocity changes from one side of the rotation axis to the other, with a smooth transition in between (which may be a slow or a fast transition). The length scale of the transition is determined by an extra parameter L . For the prior on L , we used $\log_{10}(L/\text{kpc}) \sim \text{Uniform}(-1, 2)$ for each component.

The marginal likelihood estimates for Models 1, 2.1, 2.2, and 3 for the three different kinds of velocity profiles are shown in Table 10. This shows a slight preference for model F over model V except for Model 3, which favours model V . The results also indicate that kinematic models V and F are vastly preferred over S .

However, for pragmatic reasons, we decided to prioritize Model V in the main part of the paper, similar to Mackey et al. (2019b) but different from Lewis et al. (2023), who presented model F . One reason for this is that, overall, Model V has a greater precedent in the literature. Another is that the posterior distributions are significantly more complex under the F model, due to the sudden transition from one side of M31 to the other when the L parameter is small. This complicates the interpretation and the summaries of the posterior distributions significantly. Importantly, none of the substantial conclusions of the paper (the evidence for Models 2.1 and 3 being the highest, and the inferred orientation angles of the rotational components) are affected by this choice.